High Detectivity All-Printed Organic Photodiodes

*Adrien Pierre, Igal Deckman, Pierre Balthazar Lechêne, and Ana Claudia Arias**

The recent increase in utilization of image sensors[1–3] and significant development in the field of wearable and disposable sensors[4] not only demands a decrease in photodiode fabrication costs, but also requires new functional abilities such as operating at extremely low light intensities,[5,6] narrowband and broadband spectral selectivity,[7,8] lightweight, and mechanical flexibility.[9,10] Today, most of these demands cannot be fulfilled by conventional workhorse silicon photodetectors without a significant amount of processing steps to achieve heterogeneous integration.[11] The chemical tunability, mechanical properties, and printable processing of organic materials make them promising candidates for fabrication of low-cost, highly scalable, and flexible organic photodiodes (OPDs).[12] In addition, the large-area scalability of printing techniques is beneficial for photodiodes since the signal-to-noise ratio (SNR), at a given light intensity, increases with detector size.[13,14] Since the SNR depends on systems level parameters, such as the sampling bandwidth, light intensity, and photoactive area, it significantly complicates the comparison of photodetectors. For this reason, a useful figure of merit to consider is specific detectivity D^*, which is dependent on external quantum efficiency (EQE) η, the dark current density J_d, and the power spectral density (units of A^2 Hz^{-1} cm^{-2}) of other noise sources such as flicker or thermal noise, $N_{other\ noise}$, as shown in Equation 1. Azzellino et al.'s[9] mostly inkjet-printed OPDs with specific detectivity over 10^{12} cm $Hz^{0.5}$ W^{-1} and Tedde et al.'s[15] low variability partially spray-coated OPDs are a few examples of high-performance partially printed OPDs. However all OPDs reported to date rely on thermal evaporation of oxygen-sensitive metal cathodes, spin-coating, or inkjet printing on rigid substrates, all of which are not scalable deposition methods in achieving large-area coverage or high fill factor (photosensitive area/total area).[16] Here, we show that by controlling of charge selectivity of printed organic electrodes printed using industrially scalable techniques (i.e., blade coating and screen printing), we fabricated state of the art all-printed, flexible OPDs with average specific detectivities as high as 3.45×10^{13} cm $Hz^{0.5}$ W^{-1}. In addition to the high specific detectivity needed to resolve low light intensity, these OPDs are able to sustain high reverse biases. High reverse biases are used to maximize the capacity of the photodiode to capacitively store photogenerated charge, which is essential for increasing the dynamic range of image sensors.[13,14] Through optimization and characterization of the properties of each printed layer, device yield is maximized with minimal variability over large areas. The performance of all-printed photodiodes achieved here becomes comparable to silicon photodiodes used in image sensors, which have a specific detectivity of approximately $6–7 \times 10^{13}$ cm $Hz^{0.5}$ W^{-1}.[14] These results show that along with such important advantages as inexpensive fabrication and mechanical flexibility all-printed OPDs can have performance competitive with their Si-counterparts.

$$D^* = \frac{q\lambda\eta}{hc}\left(2qJ_d + N_{other\ noise}\right)^{-1/2} \frac{\mathrm{cm}\sqrt{\mathrm{Hz}}}{\mathrm{W}} \quad (1)$$

There are materials and fabrication limitations to consider when maximizing device performance and reliability that dictate the device architecture. The lack of printable low-work function conductors for a cathode demands the use of interlayers. The interlayers not only decrease cathode work function but also have hole-blocking properties, which is essential for minimization of reverse bias dark current density.[16] The interlayers are typically cast by spin coating[9,17] from solvents that are orthogonal to underlying layers. Doctor blade coating is a preferable alternative to spin coating as it is scalable to large areas and can produce large films with well-controlled uniformity.[18] Additionally, this printing technique has been shown to be a suitable deposition method for the active layer as bulk heterojunction (BHJ) morphology can be well controlled.[19] However, printing the low viscosity solutions optimized for doctor blade and spin coating on top of the hydrophobic BHJ-active layer leads to dewetting.[20] Screen printing mediates this issue as it is highly scalable and the high viscosity of the pastes minimizes dewetting.[9,20] While films deposited through screen printing are too thick to be suitable for the poor conductivity of low-work function interlayers, conventional high-work function conductors can be readily printed. Consequently, an inverted structure offers a better route to achieve printed devices since the cathode interlayer may be deposited on the bottom electrode while the top electrode uses commonplace printable high-work function materials.

Here, we have developed and characterized a printing process, shown in **Figure 1**a, that allows the fabrication of high yield, high-performance flexible OPD arrays. The cathode is formed by a blade-coated layer of poly(3,4-ethylenedioxythiophene):poly(styrenesulfonate) (PEDOT:PSS) on a polyethylene naphthalate (PEN) substrate, resulting in a sheet resistance of approximately 700 Ω/□. A low-work function cathode is achieved with a blade-coated layer of ethoxylated polyethylenimine (PEIE) on top of the PEDOT:PSS. The active layer blade coated on top of the cathode is a BHJ blend of poly[*N*-9′-heptadecanyl-2,7-carbazole-*alt*-5,5-(4′,7′-di-2-thienyl-2′,1′,3′-benzothiadiazole)] (PCDTBT) and [6,6]-phenyl C_{71}-butyric acid methyl ester ($PC_{71}BM$). This blend material was chosen because

A. Pierre, Dr I. Deckman, Dr P. B. Lechêne, Prof. A. C. Arias
Electrical Engineering and Computer Sciences
University of California Berkeley
Berkeley, CA 94720, USA
E-mail: acarias@eecs.berkeley.edu

DOI: 10.1002/adma.201502238

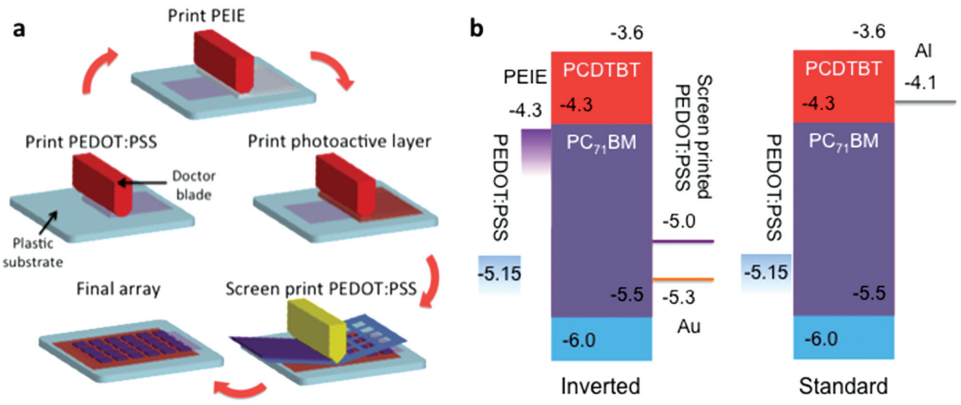

Figure 1. a) Fabrication process of all-printed organic photodiodes (OPDs). b) Band diagram of all-printed OPD structure (inverted geometry with PEDOT:PSS top anode) and other partially printed devices.

it is known to be very efficient at generating free-carriers[21,22] and have good environmental stability.[23] Additionally, low- and high-molecular-weight PCDTBT show comparable device performance in these blends.[24] This insensitivity allows the use of low-molecular-weight PCDTBT (M_n 5.99 kDa, PDI 2.24) to enable high solution concentrations, increasing the range of active layer thicknesses. Device fabrication is finished by screen printing an array of anodes of PEDOT:PSS, a well-known hole selective electrode, into the desired shape. The optimal all-printed OPD device structure with the corresponding band diagram is shown in Figure 1b with an anode and cathode work function of 5 and 4.3 eV, respectively. It is also possible to fabricate mostly printed inverted and standard geometry OPDs with evaporated gold or aluminum top electrodes, respectively, which will be compared to the all-printed devices later on. The role of the interlayer work function, active layer thickness, and choice of electrodes on device performance is investigated in order to fabricate OPDs with high specific detectivity at high reverse bias.

Poor printing reliability has been a limiting factor for improving device yield (the percentage of properly functioning devices) and variability, with few reports of partially printed OPDs demonstrating consistent performance over centimetric areas.[15] The main challenge in printing is the uniform deposition of thin interlayers[25] and patterned electrodes without shorting through underlying layers.[20] It has been shown that spin coating PEIE on top of PEDOT:PSS decreases its work function by 1.3 eV.[17] However, very few accounts of variable work function tunability without modification of the interlayer molecule have been demonstrated through any deposition process.[25] The work function of blade-coated PEDOT:PSS/PEIE cathode, which is significantly more scalable than spin coating, may be fine-tuned by changing the weight concentration of PEIE in the blade-coated solution as summarized by Kelvin probe measurements in **Figure 2**a. By changing the PEIE solution concentration between 0.05% and 1 wt%, we were able to lower the work function of PEDOT:PSS from 5.15 eV to anywhere between 4.6 and 4.1 eV. Kelvin probe force microscopy shows uniform work function modification for all measured PEIE coatings on PEDOT:PSS. Figure 2b shows blade-coated films of 0.4 wt% PEIE on PEDOT:PSS with 4.7 nm RMS roughness and 29 meV variability in work function. Figure 2c is a map of work function measurements conducted on different areas of 0.4 wt% PEIE coated on PEDOT:PSS cathode. From this map, good uniformity of work function over centimetric scales can be seen. This high homogeneity in work function seen on both the macro- and microscale indicates the absence of pinholes and other non-uniformities that lead to variability in device characteristics. While the work function of the screen-printed PEDOT:PSS paste on top of the active layer is not tuned, it is still important to ensure good printing reliability as shown by the uniform array in Figure 2d. The high viscosity (see Figure S1, Supporting Information) of the paste results in only 10–15 µm dewetting from the defined edge of the pattern, which is insignificant compared to the 450 µm defined width of each pixel. The homogeneity and work function tunability of the electrodes established by printing allow a high degree of control through which device performance may be optimized.

The reliability of our printing process allows us to examine the effect of cathode work function on device performance for the all-printed OPDs (see band diagram with PEDOT:PSS anode in Figure 1b). The dependence of EQE and dark current density on the PEDOT:PSS/PEIE cathode work function of these devices are summarized in **Figure 3**a (see Figure S2, Supporting Information for current–voltage characteristics). The PEDOT:PSS cathode work function without PEIE, 5.15 eV, creates a unipolar hole-transporting photoconductor that results in high dark current density and low EQE at –5 V bias. Lowering the work function to 4.6 eV by printing 0.05 wt% PEIE in solution significantly improves EQE to 67% but still has approximately the same high dark current density. Decreasing the cathode work function to 4.3 eV by printing 0.4 wt% PEIE in solution retains about the same EQE as the device with a 4.6 eV work function electrode, but drastically reduces the dark current density to values below 1 nA cm^{-2}. Further decreasing the cathode work function to 4.1 eV by increasing the concentration to 1 wt% PEIE in solution results in approximately the same dark current density but significantly lower EQE. Initially decreasing the work function of PEDOT:PSS results in an increase in EQE as an ohmic contact is established between the cathode and electron acceptor. However, approximately the same high dark current density as the device without PEIE is retained because the cathode lacks carrier selectivity, permitting hole transport. The abrupt decrease in

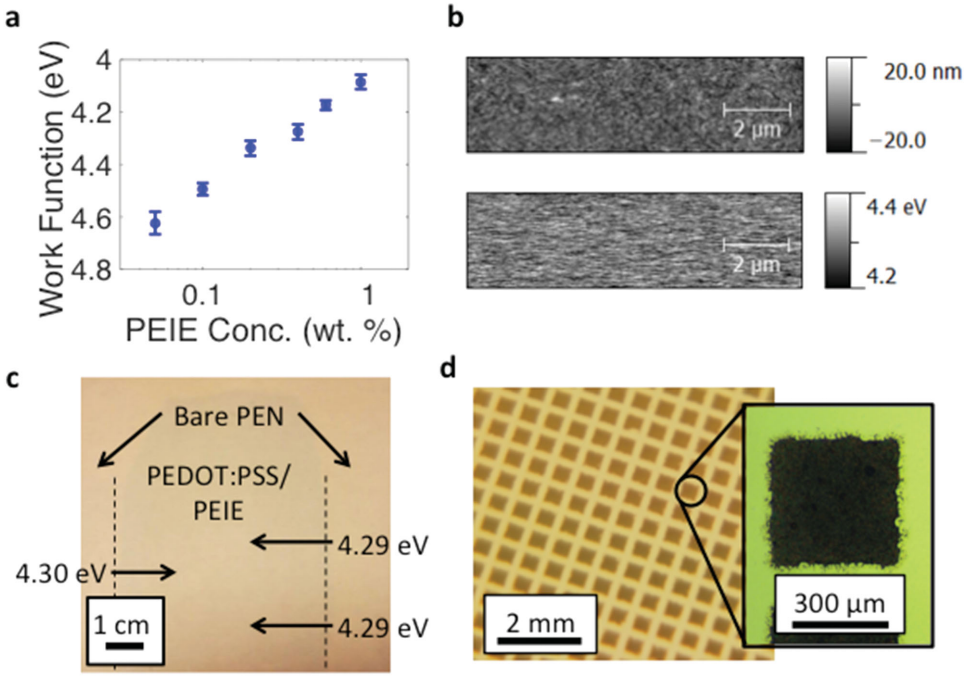

Figure 2. a) Work function of PEDOT:PSS measured using Kelvin probe force microscopy (KFM) as a function of PEIE solution concentration in 2-methoxyethanol. b) AFM (upper panel) and KFM (lower panel) measurements on PEDOT:PSS coated with a 0.4 wt% solution of PEIE in Figure 2a. c) Photograph of printed cathode in Figure 2b with KFM results measured at several locations. d) Optical microphotographs showing an array of patterned anode electrodes of an all-printed OPD array.

dark current density with decreasing the work function is attributed to the thickness-dependent hole-blocking properties of PEIE,[26] leading to the OPD with the 4.3 eV cathode showing optimal detectivity (high EQE and low dark current density). However, using a higher weight concentration of 1 wt% PEIE in solution to further decrease work function leads to a significant

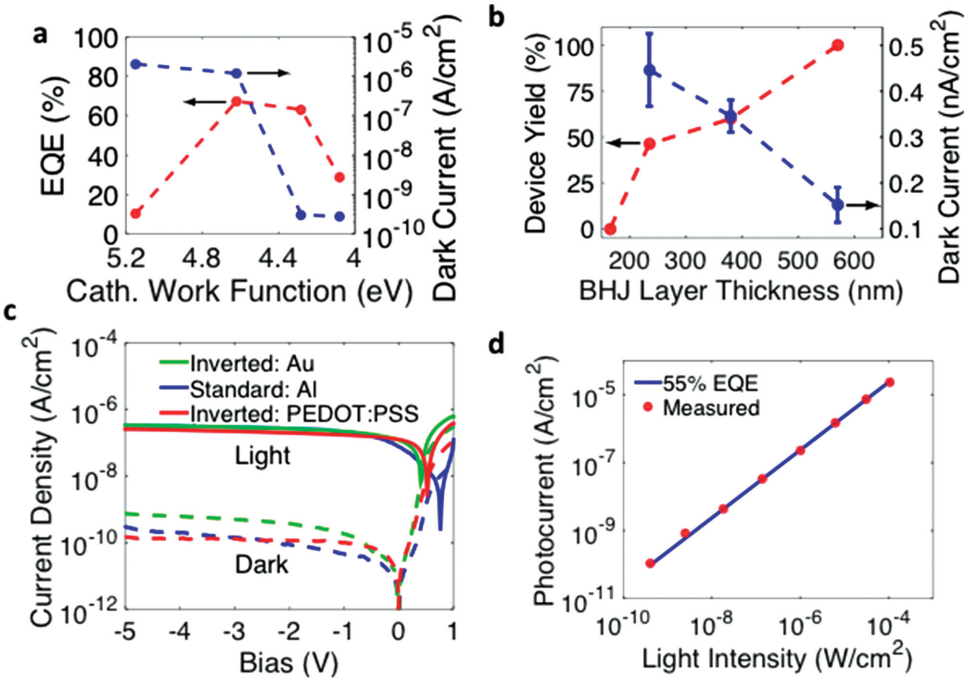

Figure 3. a) All-printed OPD (Figure 1b) mean external quantum efficiency (EQE) and dark current dependence on PEDOT:PSS/PEIE cathode work function deposited in Figure 2a. b) All-printed OPD device yield at an applied reverse bias field of 88 kV cm^{-1} and the corresponding dark current for functional devices. c) Current–voltage characteristics of devices illustrated in Figure 1b with 570 nm thick active layers under dark and light conditions at 532 nm and 1.03 μW cm^{-2}. d) Dynamic response of all-printed OPD at 532 nm biased at −5 V.

Table 1. Organic photodetector characteristics of the various structures illustrated in Figure 3b. Measurements were performed under 1.03 μW cm^{-2} at 532 nm at an applied reverse bias field of 88 kV cm^{-1} in air without encapsulation.

Device geometry	Cathode/Work function [eV]	Anode/Work function [eV]	Active layer thickness [nm]	EQE [%]/Bias [V]	J_{dark} [pA cm^{-2}]/Bias [V]	D^* (cm $Hz^{0.5}$ W^{-1})/Bias [V]
Inverted	PEDOT:PSS + PEIE/4.3	Screen-printed PEDOT:PSS/5	235	61/−2.06	440/−2.06	2.2×10^{13}/−2.06
Inverted	PEDOT:PSS + PEIE/4.3	Screen-printed PEDOT:PSS/5	380	69/−3.33	350/−3.33	2.8×10^{13}/−3.33
Inverted	PEDOT:PSS + PEIE/4.3	Screen-printed PEDOT:PSS/5	570	55/−5	150/−5	3.4×10^{13}/−5
Inverted	PEDOT:PSS + PEIE/4.3	Au/5.3	570	75/−5	740/−5	2.1×10^{13}/−5
Standard	Al/4.1	PEDOT:PSS/5.15	570	76/−5	280/−5	3.4×10^{13}/−5

drop in EQE as a result of the insulating nature of PEIE, which causes accumulated charges to recombine at the PEIE/active layer interface and making it a poor electron extractor.[27] Consequently, it is important to focus on optimizing charge selectivity for both carriers at the cathode. This is especially important when depositing interlayers as decreasing the cathode's work function to the maximum extent does not necessarily lead to the best OPD detectivity.

The thickness of the BHJ layer has been shown to influence device yield and dark current,[1,10,20] making it an important parameter to control. **Table 1** shows all-printed OPD performance for several film thicknesses at a constant applied field of 88 kV cm^{-1} (corresponding to 5 V across 570 nm). Figure 3b shows the yield (the percentage of devices, which are not shorted and exhibit photodiode behavior) and dark current density for the all-printed OPDs for various BHJ layer thicknesses. A BHJ-active layer thickness of 570 nm, the maximum thickness as limited by the solubility of the donor and acceptor in solution, exhibits perfect yield for 23 measured devices. Thinner active layers resulted in lower yields with the common failure being soft breakdown past a certain reverse bias (see Figure S3, Supporting Information). For functional devices under the applied field, dark current density decreases for increasing thickness. Film imperfections have a more significant effect for thinner BHJ layers, resulting in more leakage paths that increase dark current density under reverse bias and the likelihood of breakdown. Additionally, the built-in field resulting from the asymmetry in work function between the electrodes increases with thinner BHJ layers. This renders devices more susceptible to increased dark current density and breakdown even when the applied reverse bias is scaled to BHJ layer thickness. It should be noted the effect of BHJ layer thickness on dark current density is orders of magnitude less significant than the work function of the cathode as seen in Figure 3a, which underpins the importance of carrier selectivity at interfaces. While the dark current levels were too low for direct noise measurements, the noise spectral density from the photocurrent is found to be flat (no flicker noise behavior) and in close agreement with the theoretical shot noise (see Figure S4, Supporting Information). This observation suggests minimal noise generation from other sources such as trap states, validating the assumptions in Equation 1. Using this equation, the thickest devices offer the highest average specific detectivity of 3.4×10^{13} cm $Hz^{0.5}$ W^{-1} as a result of their low dark current density.

The top electrodes in OPDs have traditionally been thermally evaporated[2,4,6–8,16,28] and therefore constitute a benchmark for printed electrodes. Thermally evaporated top metal electrodes in both inverted and standard device geometries are compared to the all-printed OPD for 570 nm thick active layers. The gold electrode (5.3 eV) has a lower hole barrier than printed PEDOT:PSS (5 eV) while the aluminum electrode (4.1 eV) has a lower electron barrier than the printed cathode (4.3 eV) as seen in the band diagrams of Figure 1b. The inverted geometry devices with gold electrodes exhibit on average an EQE of 75% at −5 V, greater than the 55% seen in the all-printed OPD as summarized in Table 1. However, the gold electrode OPD's dark current density of 740 pA cm^{-2} is much larger compared to the all-printed devices of 150 pA cm^{-2}. A standard geometry device with an evaporated aluminum electrode has an EQE of 76% at −5 V, similar to the inverted gold anode device, and a dark current density of 280 pA cm^{-2}, which is still higher than that of the all-printed OPD. The EQE and dark current values of our standard devices are similar to other OPDs fabricated from spin coating using the same materials, layer thicknesses, and device architecture.[29] Looking at the *J*–*V* curves shown in Figure 3c, the differential shunt resistance of the dark current at −5 V of the all-printed OPD, 1×10^{11} Ω cm^2, is significantly higher than that of the OPDs with aluminum or gold top electrodes, 1.2×10^{10} and 8.7×10^{9} Ω cm^2, respectively. The high shunt resistance of the all-printed OPD indicates that the device's lower dark current density is the result of a low density of defect-induced traps at the active layer-electrode interface, which minimizes parasitic leakage paths.[30] Consequently, the higher dark current density of the OPDs with metal electrodes is believed to be the result of the diffusion of evaporated metal into the active layer, which is especially pronounced for gold.[31] Additionally, the hydrophobicity of the active layer could prevent the aqueous screen-printed PEDOT:PSS solution from diffusing into small imperfections in the active layer. The lower EQE of the all-printed OPD compared to either OPD with low charge injection barrier metal electrodes is in accordance to the finding that higher anode and lower cathode work function electrodes in organic diodes are more efficient at charge collection.[32] Despite the inferior charge collection abilities of all-printed OPDs, they show a linear dynamic range over five orders of magnitude, with an average EQE of 55% as shown in Figure 3d. Devices fabricated from a thinner active layer (235 nm) show 3-dB cutoff frequencies of 5 and 50 kHz when biased at −2.06 and −5 V, respectively (see Figure S5 and Table S1, Supporting Information). This jump in cutoff frequency by an order of magnitude with applied bias, which normally varies linearly with bias,[33] and the higher frequency

response for similar devices with an aluminum cathode[29] also suggest that carrier extraction at the electrodes could be a limiting factor for the all-printed devices. Albeit the lower aluminum cathode and higher gold anode work functions that improve carrier extraction, devices with a thermally evaporated top electrode exhibit marginally lower detectivities at higher reverse biases than all-printed OPDs as a result of their high dark current.

Operational bias, stability, and device variability are as important as standard photodiode performance metrics when designing devices for systems level applications. The dynamic range of image sensors is determined by the well capacity of the photodiode to store photogenerated charge Q_{well} according to Equation (2), where C_{PD}, V_{RB}, ε, t_{OPD}, $E_{applied}$ represent OPD capacitance, reverse bias, dielectric permittivity, active layer film thickness, and applied electric field, respectively.[13,14] In order to augment the well capacity, $E_{applied}$ can be increased by either increasing V_{RB} or thinning t_{OPD}. **Figure 4**a shows that our all-printed OPD offers higher specific detectivity at higher applied fields, maximizing well capacity, and thus dynamic range, in comparison to other OPDs in the literature (assuming dielectric constant to be similar between the various BHJ-active layers).[1,4,6–10,20,28,34] To quantify the stability of the device's specific detectivity, it is important to examine the effect of bias stress since photodiodes are continuously biased in most light-sensing systems.[4,13,14] The all-printed OPDs tested in air, which were initially left in the dark for 24 h, were stable for 3–4 h when continuously biased at −5 V with simultaneous periodic light-dark exposure (50% duty cycle) as shown in Figure 4b. However, Figure 4c shows a lengthy periodic light exposure of 20 h led to a significant increase in both mean EQE, from 55% to 70%, and mean dark current density, from 150 to 720 pA cm^{-2}, for 23 OPD pixels (each with 0.16 mm^2 photoactive area) measured over an area of 4.5 cm^2 regardless of whether the OPDs were electrically biased. This corresponds to a mean drop in specific detectivity from 3.45×10^{13} to 2.01×10^{13} cm Hz$^{0.5}$ W^{-1} while the coefficient of variation (standard deviation/mean) decreases from 15% to 9%. It is believed that the simultaneous increase in EQE and dark current density is the result of photo-oxidation mechanisms, which dope the active layer and have been shown to increase both on and off current in organic thin film transistors.[35] This is supported by the observation that devices left in nitrogen exposed to light continuously for several months exhibit negligible change in EQE and dark current density (see Figure S6, Supporting Information). The EQE spectrum of the post-light biased all-printed OPD in Figure 4d shows more than 50% EQE through most of the visible spectrum. The significant increase in EQE from 0 to −1 V is a result of the inherent low charge mobility of PCDTBT:PC$_{71}$BM BHJ blends, which is further exacerbated by thermal annealing[36] during the printing process. While the high optical density of thick active layers typically show flat EQE spectra,[29] the gradual decrease in EQE between 500 and 600 nm is a result of increased absorption in our PEDOT:PSS cathode for wavelengths above 500 nm.[37] Despite the decrease of specific

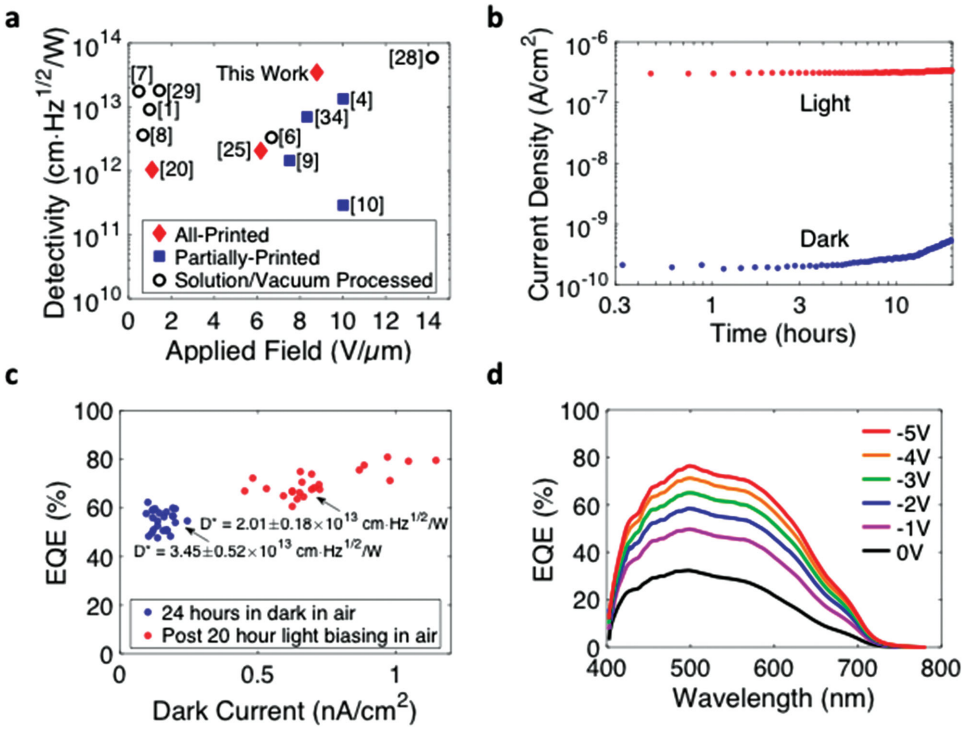

Figure 4. a) Comparison of specific detectivity at various applied fields (reverse bias voltage/film thickness) for all-printed OPDs and other OPDs published in the literature calculated according to Equation (1). b) An all-printed OPD (Figure 1b) biased continuously at −5 V for 20 h in air alternating between light (532 nm) and dark with a 50% duty cycle. c) Scatter plot of EQE, dark current and detectivity of all-printed OPDs that were left for 24 h in the dark in air prior to measurement and exposed to the same conditions in Figure 4b. d) EQE spectral response of post-biased OPD under various applied reverse biases under 3–6 μW cm^{-2}.

detectivity over the course of several hours, the stability of our devices when kept long term in the glovebox and short term in air suggests that even rudimentary encapsulation could preserve as-fabricated device performance for a significantly longer amount of time as has been shown for organic photovoltaic cells.[23]

$$Q_{well} = C_{PD}V_{RB} \propto \varepsilon V_{RB} / t_{OPD} = \varepsilon E_{applied} \quad (2)$$

In summary, highly scalable and inexpensive manufacturing techniques such as doctor blade coating and screen printing can be used to deposit each layer of an OPD in order to create high-performance devices on plastic substrates. These scalable printing techniques are precise enough to tailor the performance of the OPDs over large areas with good uniformity. Specifically, the PEIE interlayer's hole-blocking properties has a profound impact on dark current and is well controlled through doctor blade coating. Controlling active layer thickness ensures good reliability and minimized dark current even under large applied fields needed to maximize well capacity. Finally, all-printed OPDs display high detectivity as a result of their low dark current density in comparison to OPDs with thermally evaporated metal electrodes. Through these considerations we demonstrate high yield low variability all-printed OPD arrays that achieve average specific detectivities as high as 3.45×10^{13} cm $Hz^{0.5}$ W^{-1} under a bias of –5 V. The detectivity of these all-printed OPDs is competitive with conventional inorganic photodiodes and can pave the way to inexpensive, ubiquitous and large area optical systems.

Experimental Section

Device Fabrication: Teijin films provided the PEN substrates used for the OPDs. A 50 W plasma was applied through a stencil to define a central hydrophilic strip onto which PEDOT:PSS (Sigma–Aldrich 739316) was doctor bladed at 1.6 cm s^{-1} with a 200 µm gap, using a Zehntner ZUA 2000 blade coater, then annealed for 10 min at 120 °C. The samples were then transferred to a nitrogen glove box where PEIE was coated onto PEDOT:PSS at 1.6 cm s^{-1} with a 100 µm gap then annealed for 10 min at 100 °C. A 1:3 PCDTBT(St-Jean Photochimie):$PC_{71}BM$(Solaris Chem) solution dissolved to 80 mg mL^{-1} in chlorobenzene was blade coated on a 40 °C platform at 2.8 cm s^{-1} with a 200 µm gap and maintained at that temperature for 2 h. The sample was pre-annealed at 120 °C for 10 min before transferring back to air to have 0.16 mm^2 PEDOT:PSS (4:1 mixture of Agfa Gevaert EL-P5015: Clevios P VP Al 4083) pixels screen printed at 10 cm s^{-1} using an ASYS ASP 01M screen printer. Devices were dried out under vacuum for 10 min before being annealed in a glove box at 120 °C for 5 min. Devices with aluminum or gold electrodes were deposited by thermal evaporation at a base pressure of 5×10^{-6} Torr at 0.5 nm s^{-1}.

Device Characterization: A Veeco 6M Dektak profiler measured film thickness while an NT-MDT NTEGRA Prima AFM measured topography and work function. An Agilent B1500a semiconductor parameter analyzer measured current–voltage characteristics except for EQE measurements during which a Keithley 2400 was used. A shielded probe station was used to ensure a dark and low-noise environment. Open measurements and a Hamamatsu S2387-66R calibrated silicon photodiode were used to ensure faithful dark and light current readings. An Agilent 3567A power spectrum analyzer, Electro Optical Components DHPCA-100 transimpedance amplifier and Tektronix TDS3014 oscilloscope were used for noise and frequency measurements.

Supporting Information

Supporting Information is available from the Wiley Online Library or from the author.

Acknowledgements

This work was supported in part by Systems on Nanoscale Information fabriCs (SONIC), one of the six SRC STARnet Centers, sponsored by MARCO and DARPA. This work was also supported by the National Science Foundation under Cooperative Agreement No. EEC-1160494 and by the NSF Graduate Fellowship Research Program under Grant No. DGE-1106400. The authors acknowledge Prof. Salahuddin for access to the atomic and Kelvin probe force microscope and Prof. Rabaey for discussion on the characterization of these devices.

Received: May 10, 2015
Revised: July 14, 2015
Published online: September 23, 2015

[1] T. N. Ng, W. S. Wong, M. L. Chabinyc, S. Sambandan, R. A. Street, *Appl. Phys. Lett.* **2008**, *92*, 213303.
[2] T. Rauch, M. Boberl, S. F. Tedde, J. Furst, M. V. Kovalenko, G. Hesser, U. Lemmer, W. Heiss, O. Hayden, *Nat. Photonics* **2009**, *3*, 332.
[3] S. Nau, C. Wolf, S. Sax, E. J. W. List-Kratochvil, *Adv. Mater.* **2015**, *27*, 1048.
[4] C. M. Lochner, Y. Khan, A. Pierre, A. C. Arias, *Nat. Commun.* **2014**, *5*, 5745.
[5] Y. Fang, J. Huang, *Adv. Mater.* **2015**, *27*, 2804.
[6] M. Binda, A. Iacchetti, D. Natali, L. Beverina, M. Sassi, M. Sampietro, *Appl. Phys. Lett.* **2011**, *98*, 073303.
[7] A. Armin, R. D. Jansen-van Vuuren, N. Kopidakis, P. L. Burn, P. Meredith, *Nat. Commun.* **2015**, *6*, 6343.
[8] X. Gong, M. Tong, Y. Xia, W. Cai, J. S. Moon, Y. Cao, G. Yu, C.-L. Shieh, B. Nilsson, A. J. Heeger, *Science* **2009**, *325*, 1665.
[9] G. Azzellino, A. Grimoldi, M. Binda, M. Caironi, D. Natali, M. Sampietro, *Adv. Mater.* **2013**, *25*, 6829.
[10] G. Pace, A. Grimoldi, D. Natali, M. Sampietro, J. E. Coughlin, G. C. Bazan, M. Caironi, *Adv. Mater.* **2014**, *26*, 6773.
[11] H. C. Ko, M. P. Stoykovich, J. Song, V. Malyarchuk, W. M. Choi, C.-J. Yu, J. B. Geddes Iii, J. Xiao, S. Wang, Y. Huang, J. A. Rogers, *Nature* **2008**, *454*, 748.
[12] A. C. Arias, J. D. MacKenzie, I. McCulloch, J. Rivnay, A. Salleo, *Chem. Rev.* **2010**, *110*, 3.
[13] R. A. Street, *Technology and Applications of Amorphous Silicon*, *37*, Springer-Verlag, Berlin, Heidelberg, Germany **2000**.
[14] G. C. Holst, T. S. Lomheim, *CMOS/CCD Sensors and Camera Systems*, *408*, JCD Publishing, FL, USA **2007**.
[15] S. F. Tedde, J. Kern, T. Sterzl, J. Furst, P. Lugli, O. Hayden, *Nano Lett.* **2009**, *9*, 980.
[16] K.-J. Baeg, M. Binda, D. Natali, M. Caironi, Y.-Y. Noh, *Adv. Mater.* **2013**, *25*, 4267.
[17] Y. H. Zhou, C. Fuentes-Hernandez, J. Shim, J. Meyer, A. J. Giordano, H. Li, P. Winget, T. Papadopoulos, H. Cheun, J. Kim, M. Fenoll, A. Dindar, W. Haske, E. Najafabadi, T. M. Khan, H. Sojoudi, S. Barlow, S. Graham, J. L. Bredas, S. R. Marder, A. Kahn, B. Kippelen, *Science* **2012**, *336*, 327.
[18] A. Pierre, M. Sadeghi, M. M. Payne, A. Facchetti, J. E. Anthony, A. C. Arias, *Adv. Mater.* **2014**, *26*, 5722.

[19] L. J. Richter, D. M. DeLongchamp, F. A. Bokel, S. Engmann, K. W. Chou, A. Amassian, E. Schaible, A. Hexemer, *Adv. Energy Mater.* **2014**, *5*, 1400975.
[20] L. L. Lavery, G. L. Whiting, A. C. Arias, *Org. Electron.* **2011**, *12*, 682.
[21] S. H. Park, A. Roy, S. Beaupre, S. Cho, N. Coates, J. S. Moon, D. Moses, M. Leclerc, K. Lee, A. J. Heeger, *Nat. Photonics* **2009**, *3*, 297.
[22] B. Lechêne, G. Perrier, K. Emmanouil, S. Kennou, B. Bouthinon, R. de Bettignies, *Sol. Energy Mater. Sol. Cells* **2014**, *120*, 709.
[23] C. H. Peters, I. T. Sachs-Quintana, W. R. Mateker, T. Heumueller, J. Rivnay, R. Noriega, Z. M. Beiley, E. T. Hoke, A. Salleo, M. D. McGehee, *Adv. Mater.* **2012**, *24*, 663.
[24] J. W. Kingsley, P. P. Marchisio, H. Yi, A. Iraqi, C. J. Kinane, S. Langridge, R. L. Thompson, A. J. Cadby, A. J. Pearson, D. G. Lidzey, R. A. L. Jones, A. J. Parnell, *Sci. Rep.-UK* **2014**, *4*, 5286.
[25] A. Falco, A. M. Zaidi, P. Lugli, A. Abdellah, *Org. Electron*, *23*, 186.
[26] Y. H. Kim, T. H. Han, H. Cho, S. Y. Min, C. L. Lee, T. W. Lee, *Adv. Funct. Mater.* **2014**, *24*, 3808.
[27] P. Li, G. Wang, L. Cai, B. Ding, D. Zhou, Y. Hu, Y. Zhang, J. Xiang, K. Wan, L. Chen, K. Alameh, Q. Song, *Phys. Chem. Chem. Phys.* **2014**, *16*, 23792.
[28] F. Guo, B. Yang, Y. Yuan, Z. Xiao, Q. Dong, Y. Bi, J. Huang, *Nat. Nanotechnol.* **2012**, *7*, 798.
[29] A. Armin, M. Hambsch, I. K. Kim, P. L. Burn, P. Meredith, E. B. Namdas, *Laser Photonics Rev.* **2014**, *8*, 924.
[30] J. Nelson, *The Physics of Solar Cells*, Imperial College Press, London **2003**.
[31] R. Nowicki, *Gold Bull.* **1982**, *15*, 21.
[32] P. de Bruyn, A. H. P. van Rest, G. A. H. Wetzelaer, D. M. de Leeuw, P. W. M. Blom, *Phys. Rev. Lett.* **2013**, *111*, 186801.
[33] Q. Lin, A. Armin, D. M. Lyons, P. L. Burn, P. Meredith, *Adv. Mater.* **2015**, *27*, 2060.
[34] F. Arca, S. F. Tedde, M. Sramek, J. Rauh, P. Lugli, O. Hayden, *Sci. Rep.* **2013**, *3*, 1324.
[35] L. A. Majewski, J. W. Kingsley, C. Balocco, A. M. Song, *Appl. Phys. Lett.* **2006**, *88*, 222108.
[36] Z. M. Beiley, E. T. Hoke, R. Noriega, J. Dacuna, G. F. Burkhard, J. A. Bartelt, A. Salleo, M. F. Toney, M. D. McGehee, *Adv. Energy Mater.* **2011**, *1*, 954.
[37] Y. H. Kim, C. Sachse, M. L. Machala, C. May, L. Müller-Meskamp, K. Leo, *Adv. Funct. Mater.* **2011**, *21*, 1076.

ADVANCED MATERIALS

Supporting Information

for *Adv. Mater.*, DOI: 10.1002/adma.201502238

High Detectivity All-Printed Organic Photodiodes

*Adrien Pierre, Igal Deckman, Pierre Balthazar Lechêne, and Ana Claudia Arias**

Supporting Information

Title: High Detectivity All-Printed Organic Photodiodes

*A. Pierre, I. Deckman, P.B. Lechêne, A.C. Arias**

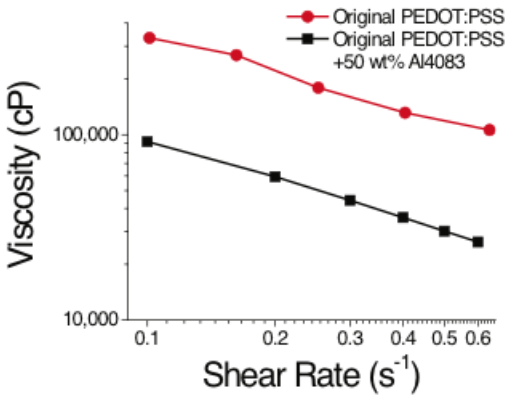

Figure S1: Viscosity of screen printed PEDOT:PSS undiluted (Courtesy of Agfa Gevaert) and diluted in CLEVIOS PVP AI 4083.

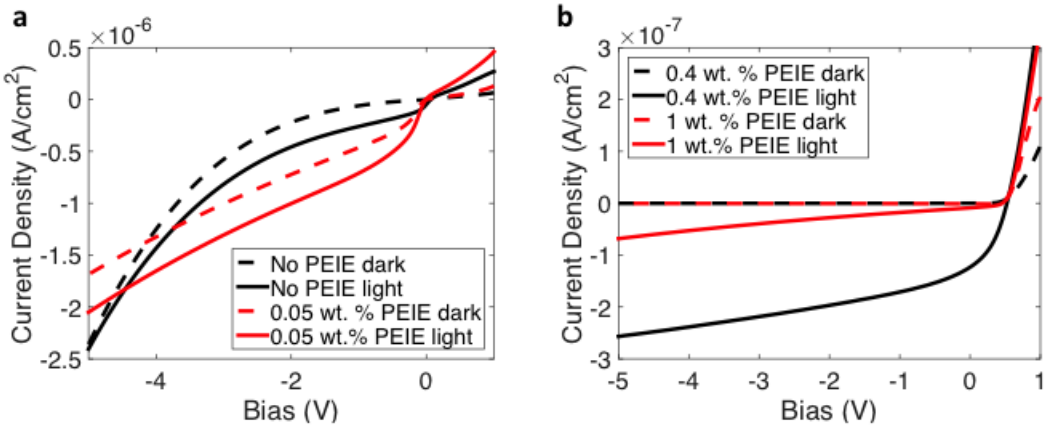

Figure S2: a) Light (1 μW/cm² @ 532 nm) and dark current-voltage characteristics of all-printed OPDs with no PEIE and 0.05 wt. % PEIE solution deposited for the cathode. b) Light (1 μW/cm² @ 532 nm) and dark current-voltage characteristics of all-printed OPDs with 0.4 wt. % and 1 wt. % PEIE solution deposited for the cathode.

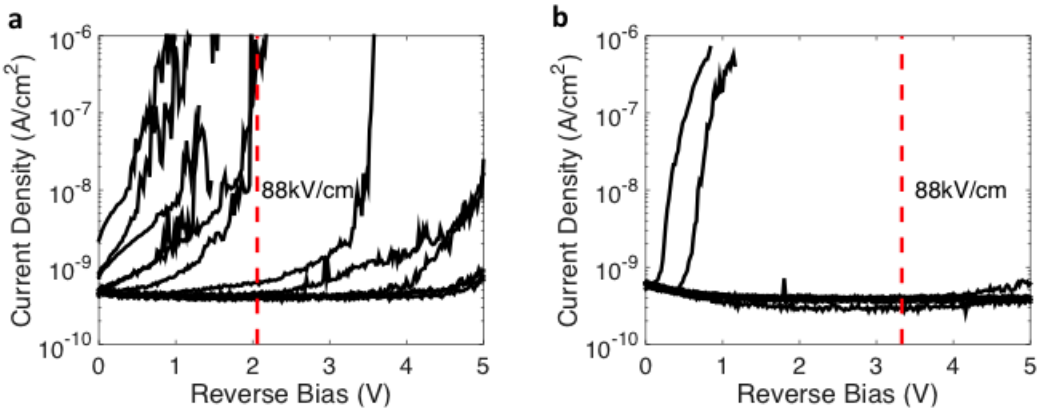

Figure S3: a) Current-voltage characteristics of all-printed OPDs with 235 nm active layer thickness under reverse bias for multiple devices. b) Current-voltage characteristics of all-printed OPDs with 380 nm active layer thickness under reverse bias for multiple devices. Device yield was taken according to whether the device broke down prior to reaching the applied field of 88 kV/cm as indicated by the red dashed line at the corresponding bias.

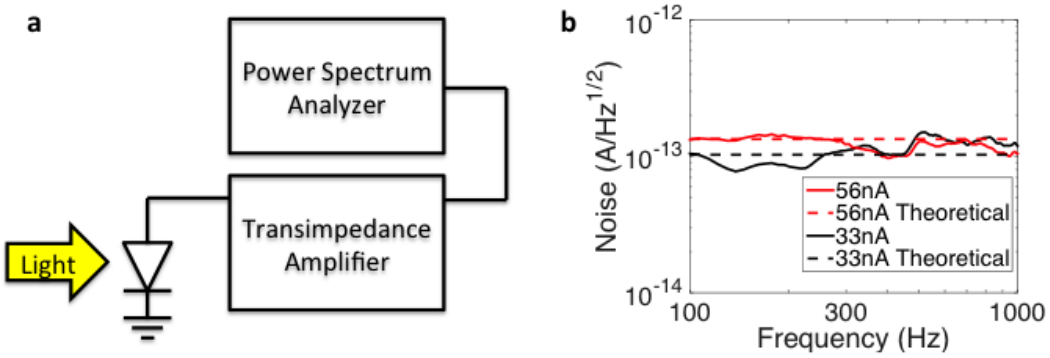

Figure S4: a) Setup for photocurrent noise measurement. b) Spectral noise density of photocurrent (33 and 56 nA) under different light intensities, for all-printed OPDs (solid lines) measured at short circuit with the corresponding theoretical value of the shot noise (dashed lines). The noise floor of the instrumentation is approximately 10^{-14} A/Hz$^{1/2}$. No different was observed when measuring photocurrent noise under reverse bias as the noise from the dark current is well below the detectable range of the instrumentation.

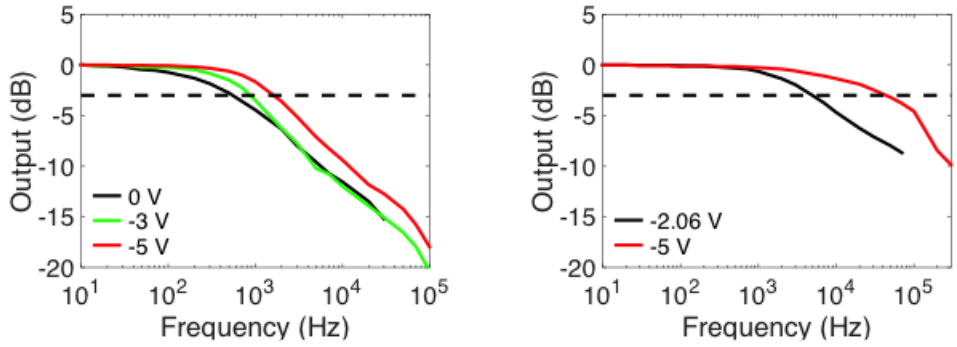

Figure S5: a) Frequency response of an all-printed OPD with a 570 nm active layer and 0.16 mm^2 active area under sine-modulated light at various biases. b) Same as a) but for a 235 nm active layer.

Table S1: All-printed OPD frequency response for various BHJ active layer thicknesses and biases.

BHJ Thickness	Bias	Applied Field	Internal Field	f_{3dB}
570 nm	0 V	0 kV/cm	12 kV/cm	500 Hz
570 nm	-3 V	53 kV/cm	65 kV/cm	1 kHz
570 nm	-5 V	88 kV/cm	100 kV/cm	2 kHz
235 nm	-2.06 V	88 kV/cm	117 kV/cm	5 kHz
235 nm	-5 V	213 kV/cm	243 kV/cm	50 kHz

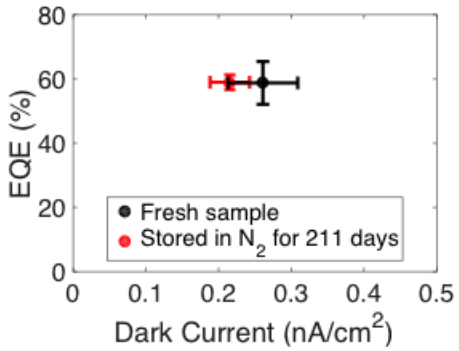

Figure S6: EQE and dark current of a batch of all-printed OPDs measured the day of fabrication and 211 days after being stored in nitrogen while exposed to ambient light.

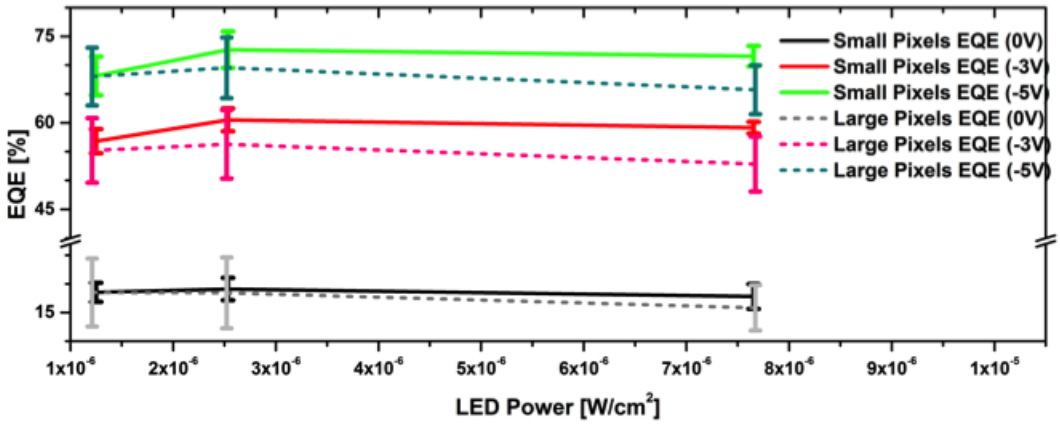

Figure S7: EQE at various light intensities (532 nm) for small (0.29 mm^2) and large (3.8 mm^2) standard geometry partially-printed devices with an evaporated aluminum top electrode.